doi.org/10.26434/chemrxiv.12844733.v1

Predicting Aqueous Stability of Solid with Computed Pourbaix Diagram using SCAN Functional

Zhenbin Wang, Xingyu Guo, Joseph H. Montoya, Jens Kehlet Nørskov

Submitted date: 21/08/2020 • Posted date: 24/08/2020

Citation information: Wang, Zhenbin; Guo, Xingyu; Montoya, Joseph H.; Nørskov, Jens Kehlet (2020): Predicting Aqueous Stability of Solid with Computed Pourbaix Diagram using SCAN Functional. ChemRxiv. Preprint. https://doi.org/10.26434/chemrxiv.12844733.v1

In this work, using the SCAN functional, we develop a simple method on top of the Materials Project (MP) Pourbaix diagram framework to accurately predict the aqueous stability of solids. We extensively evaluate the SCAN functional's performance in computed formation enthalpies for a broad range of oxides and develop Hubbard U corrections for transition metal oxides where the standard SCAN functional exhibits large deviations. The performance of the calculated Pourbaix diagram using the SCAN functional is validated with comparison to the experimental and the MP PBE Pourbaix diagrams for representative examples. Benchmarks indicate the SCAN Pourbaix diagram systematically outperforms the MP PBE in aqueous stability prediction. We further show applications of this method in accurately predicting the dissolution potentials of the state-of-the-art catalysts for oxygen evolution reaction in acidic media.

Predicting Aqueous Stability of Solid with Computed Pourbaix Diagram using SCAN Functional

Zhenbin Wang,[†] Xingyu Guo,[‡] Joseph Montoya,[¶] and Jens K. Nørskov[*,†]

[†]*CatTheory, Department of Physics, Technical University of Denmark, 2800 Kongens Lyngby, Denmark*

[‡]*Materials Science and Engineering Program, University of California San Diego, 9500 Gilman Dr, La Jolla, CA 92093, USA*

[¶]*Toyota Research Institute, Los Altos, CA 94022, USA*

E-mail: jkno@dtu.dk

Abstract

In this work, using the SCAN functional, we develop a simple method on top of the Materials Project (MP) Pourbaix diagram framework to accurately predict the aqueous stability of solids. We extensively evaluate the SCAN functional's performance in computed formation enthalpies for a broad range of oxides and develop Hubbard U corrections for transition metal oxides where the standard SCAN functional exhibits large deviations. The performance of the calculated Pourbaix diagram using the SCAN functional is validated with comparison to the experimental and the MP PBE Pourbaix diagrams for representative examples. Benchmarks indicate the SCAN Pourbaix diagram systematically outperforms the MP PBE in aqueous stability prediction. We further show applications of this method in accurately predicting the dissolution potentials of the state-of-the-art catalysts for oxygen evolution reaction in acidic media.

Introduction

Predicting aqueous stability of solids is of central importance to the development of new materials for electrochemical applications such as fuel cells, electrolyzers and Li-air batteries.[1–4] The electrode potential−pH (aka. Pourbaix) diagram maps the most stable species in an aqueous environment and has become an invaluable tool in evaluating aqueous stability. Hansen et al.[1] developed the concept of surface Pourbaix diagram to identify the most stable surface of metal cathodes under the operating conditions of oxygen reduction reaction. Persson et al.[2] proposed an efficient scheme unifying the Gibbs free energies of *ab initio* calculated solids and the experimental aqueous ions for the Pourbaix diagram construction. The advent of large computational material databases (e.g. the Materials Project, abbr. MP) has enabled high-throughput screening of materials of interest in terms of their aqueous stability.[3–5] Nevertheless, aqueous stability screening based on the current implementation of the MP Pourbaix diagram[2,5] leads to some unexpected inaccuracies. One example is selenium dioxide (SeO_2), which is incorrectly predicted to be stable in acid and water.[6] This qualitative inconsistency occurs in that the corrected formation energy of SeO_2 is an outlier in the MP data, exhibiting a large error (1.18 eV per formula unit). In the MP, a correction of 1.40 eV/O_2 is used for oxide compounds to calibrate the error in calculated formation energy, arising from the overestimated O_2 binding energy in the Perdew-Burke-Ernzerhof (PBE) functional.[7] Though this approach significantly improves the accuracy of computed formation energies and phase diagrams overall, large deviations can persist for many compounds like selenium (See Figure S1) which may affect predicted positions of equilibrium lines on the pourbaix diagram.

Since the spread of this error, even when systematically correcting formation energies, may have an impact on the positioning of aqueous phase equilibria, improving the overall accuracy of the physical methods to calculate formation energy of solids can significantly improve the reliability of aqueous stability prediction. Recently, the strongly constrained and appropriately normed (SCAN) functional has demonstrated such an improvement accuracy in both energetics and geometries.[8–11] Specifically, Zhang et al.[11] demonstrated that the formation energies of 196 binary compounds using the SCAN functional reduces the mean absolute error (MAE) to 0.1 eV/atom,

halving that of the Perdew-Burke-Ernzerhof (PBE) functional. This remarkable improvement is attributed to its satisfaction of all known exact constraints applicable to a semilocal functional.[8,9] The SCAN functional still has difficulties in accurately predicting the formation energy for transition metal compounds due to the self-interaction error.[11]

In this work, using the SCAN functional, we developed a new approach that modifies the MP Pourbaix diagram construction to predict the aqueous stability of solids. The SCAN functional with Hubbard U corrections is used to improve performance in calculated formation energy for transition metal oxides. When compared to the MP PBE Pourbaix diagram, SCAN-computed Pourbaix diagrams systematically improve the accuracy of aqueous stability predictions, and therefore enable an avenue to more reliably screen materials by this figure of merit in high-throughput computations.

Results

Formation enthalpy of oxides

Though Zhang et al.[11] investigated the formation enthalpy of 196 binary compounds using the SCAN functional, only 46 compounds are oxides, and most importantly, some oxides of technologically relevance (e.g. IrO_2 and RuO_2, both are popular oxygen evolution reaction (OER) catalysts) are not included in their benchmarking. In this work, we benchmark against a more comprehensive dataset of 114 binary oxides to demonstrate the performance of the SCAN functional in formation enthalpy calculations which are particularly important in considerations of aqueous stability. However, the SCAN functional still performs poorly in calculated formation enthalpies for 3*d* transition metal oxides (MAE = 0.205 eV/atom) due to self-interaction errors.[11,12] Using the Materials Project (MP) methods, outlined in Refs 7 and 13, we developed a set of Hubbard U corrections to aid the SCAN functional to accurately calculate formation enthalpies for transition metal (TM = V, Cr, Mn, Fe, Co, Ni, Mo) oxides (TMOs). (Table S1) These TMOs for Hubbard U corrections were selected by following the MP convention and TMOs studied in this work refer to

these seven classes of TM oxides specifically.[7,13] We note that anion corrections from the standard suite of MP corrections[7] are omitted in our approach because the SCAN functional has a very small error in the calculated O_2 binding energy (5.27 eV *vs*. experimental 5.12∼5.23 eV[14,15]). All PBE functional data used in this paper were retrieved from the MP.[5,16,17]

Figure 1 presents calculated formation enthalpies (ΔH_{calc}) of 114 binary oxides using the PBE(+U), SCAN and SCAN(+U) functionals. The mean absolute error (MAE) of ΔH_{calc} for PBE(+U), SCAN, SCAN(+U) are 0.182 eV/atom, 0.094 eV/atom and 0.072 eV/atom, respectively. The inset figure shows ΔH_{calc} of TMOs using PBE+U, SCAN and SCAN+U functionals. The non-U-corrected SCAN functional yields an MAE of 0.156 eV/atom in ΔH_{calc} and larger than 0.084 eV/atom of PBE+U. Whereas, SCAN+U significantly reduces the MAE of ΔH_{calc} from 0.156 eV/atom to 0.025 eV/atom and is also smaller than PBE+U. In addition, SCAN+U using the U fitted to binary transition-metal oxides performs well on ternary systems, achieving an MAE of 0.053 eV/atom on a benchmark of 47 ternary transition metal oxides (Figure S2).

Validation

We first benchmark our method by validating the calculated Pourbaix diagram of three examples of Ti, Ta, Se with respect to their experimental Pourbaix diagram. Since the construction of Pourbaix diagrams depends on the species included, we here use consistent species for direct comparison between experiment and computation. The primary difference between computed and experimental Pourbaix diagrams is that the chemical potentials of solids in the computed Pourbaix diagram are calculated using the SCAN(+U) functional instead of experimental data. For theoretical Pourbaix diagrams, we use experimental thermodynamic data of aqueous ions according to the integration scheme of Persson et al.[2] To further validate the accuracy of our method in aqueous stability predictions, we also generate a SCAN calculated Pourbaix diagram by computing and including all materials in the given composition space from the Materials Project. (termed "complete Pourbaix diagram") to compare with the MP PBE results. The experimental chemical potentials of solids and aqueous ions are from Refs 21, 20 and 22.

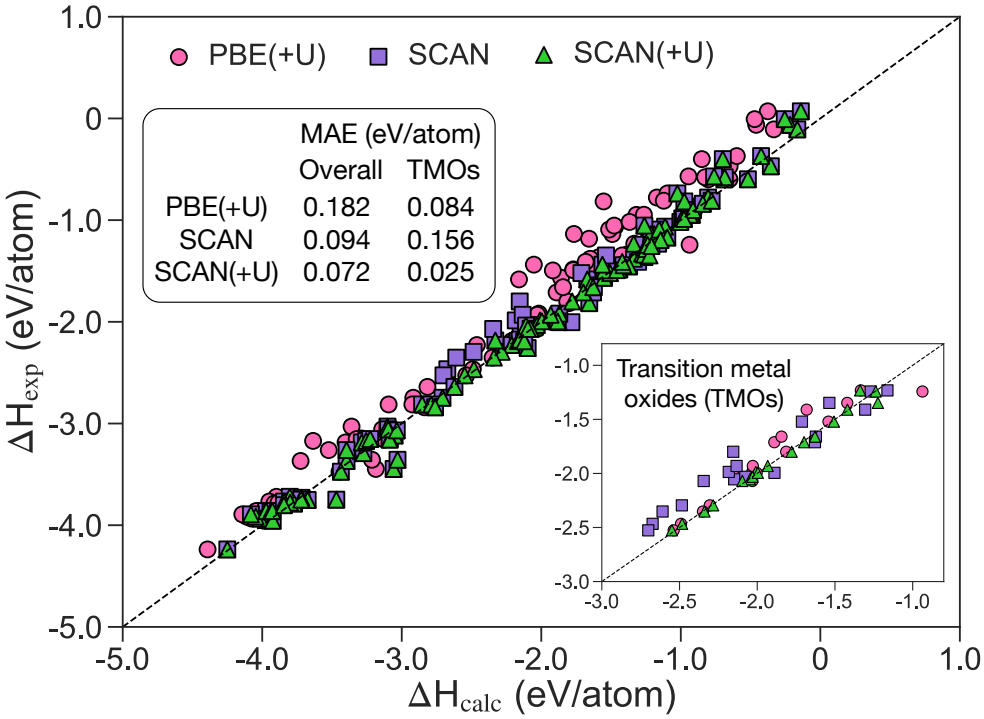

Figure 1: Experimental formation enthalpies as function of calculated formation enthalpies for 114 binary oxides. The inset shows calculations with U corrections for transition metal (TM = V, Cr, Mn, Fe, Co, Ni, Mo) oxides. PBE(+U) and experimental data were retrieved from the Materials Project[5,16,17] and Ref 18–20.

Figure 2a shows the calculated Pourbaix diagram for Ti using the SCAN functional. Compared to the experimental diagram (Figure 2b), the solid and aqueous stability regions are extraordinarily well-represented. The Ti Pourbaix diagram presented in the literature[2,23] is generally constructed without TiH_2, as shown in Figure S3a-b, where an excellent agreement between our calculated and experimental results is achieved as well. The inclusion of TiH_2 will considerably reduce the stability region of Ti^{2+} in the conventional Ti Pourbaix diagram (Figure S3a-b). In the complete Pourbaix diagram (Figure S3c), Ti_2O_7 becomes the stable phase instead of the TiO_2^{2+} in extremely oxidative environments ($E > 2.0$ V), which is consistent with experiment.[24] In the MP PBE Pourbaix diagram (Figure S3d), the predicted stability region of Ti^{2+} is much larger than that in the experimental diagram and TiO_2 dissolves to TiO_2^{2+} instead of being oxidized to Ti_2O_7 at high potentials ($E > 2.0$ V) in acid.

Figure 2c shows the calculated Ta Pourbaix diagram using the SCAN functional, which is consistent with the experimental results in Figure 2d. Tantalum pentoxide, Ta_2O_5, is barely reactive in aqueous solution and often serves as a catalyst or catalyst stabilizer for oxygen evolution in both acid and base because of its high aqueous stability.[25,26] We note that when adding the the aqueous ion TaO_2^{2+} in the Pourbaix diagram generation procedure (Figure S4a-b), Ta_2O_5 dissolves to TaO_2^{2+} in acid, contradicting experimental observations.[25,26] This is because Ta_2O_5 is corroded in concentrated hydrofluoric or alkaline media.[27] Some care has to be taken when screening aqueous stable materials for electrocatalysis, where dilute concentrations are commonly used in experiment. In the complete Pourbaix diagram (Figure S4c), high-valence tantalum oxides (e.g Ta_2O_7) and tantalum hydrides (e.g TaH_2) are predicted to be stable under highly oxidative and reductive environments, respectively. Similar results are also observed in the MP PBE Pourbaix diagram. (Figure S4d)

In the above two examples, we have verified that our method makes predictions which have similar high qualitative accuracy as MP PBE.[2,5] Next, we present an example where our results are significantly different from MP PBE. Figure 3e shows the calculated selenium Pourbaix diagram using the SCAN functional, which closely reflects the experimental diagram, shown in Figure

3f. The complete Pourbaix diagram using the SCAN functional is also the same as the experimental diagram. There is only one solid region (Se metal) in the SCAN calculated and experiment diagrams. In the MP PBE scheme, selenium oxides (SeO_2, Se_2O_5, SeO_3, SeO_4) are overstabilized in acid and appear prominently in the Pourbaix diagram, shown in Figure S5. This overstabilization results from the MP anion correction scheme, which overcorrects the calculated formation enthalpies of selenium oxides. For example, the MP anion correction shifts the PBE calculated formation enthalpy of SeO_2 from -2.111 eV/fu to -3.515 eV/fu (ΔH_{exp} = -2.334 eV/fu).

3*d* metal (Mn/Fe/Co/Ni) Pourbaix diagram

By applying U corrections on top of O_2 correction,[7,13] the MP PBE scheme provided the state-of-the-art computational 3*d* metals (M = Mn/Fe/Co/Ni) Pourbaix diagrams. (Figure S6) Nevertheless, the scheme resulted in qualitative and quantitative inaccuracies when predicting the aqueous stability for metal (oxy)hydroxides and hydrides. This is because the affine corrections of the MP scheme may over- or under-correct certain classes of materials or reference hydrogen chemical potentials in order to fix systematic errors in oxides. SCAN's accuracy in predicting the underlying thermochemistry makes affine corrections largely unnecessary, meaning that more accurate Pourbaix diagrams can likely be constructed using the simpler methodology herein going forward.

Figure 3 presents the calculated and experimental 3*d* metal (M = Mn/Fe/Co/Ni) Pourbaix diagrams. In general, the predicted solid and aqueous ion regions in the calculated diagrams are consistent with the experimental results. Two differences are noted: (1) the relative stability regions of metal oxides in the calculated diagrams are slightly different from those in experimental diagrams; (2) the stability regions of $Co(OH)_2$ and $Ni(OH)_2$ are much larger than those in experiment. These differences can be attributed to the uncertainties of the SCAN+U functional in calculating redox reactions energies of $M^{2+} \rightarrow M^{3+} \rightarrow M^{4+}$. In particular, the relatively large differences between computation and experiment for Co and Ni is likely due to the influence of magnetic configurations.[28,29] For example, the ground state magnetic configuration of CoO, Co_3O_4 and NiO is antiferromagnetic.[28,29] Given it is too computationally expensive and complicate to calculate

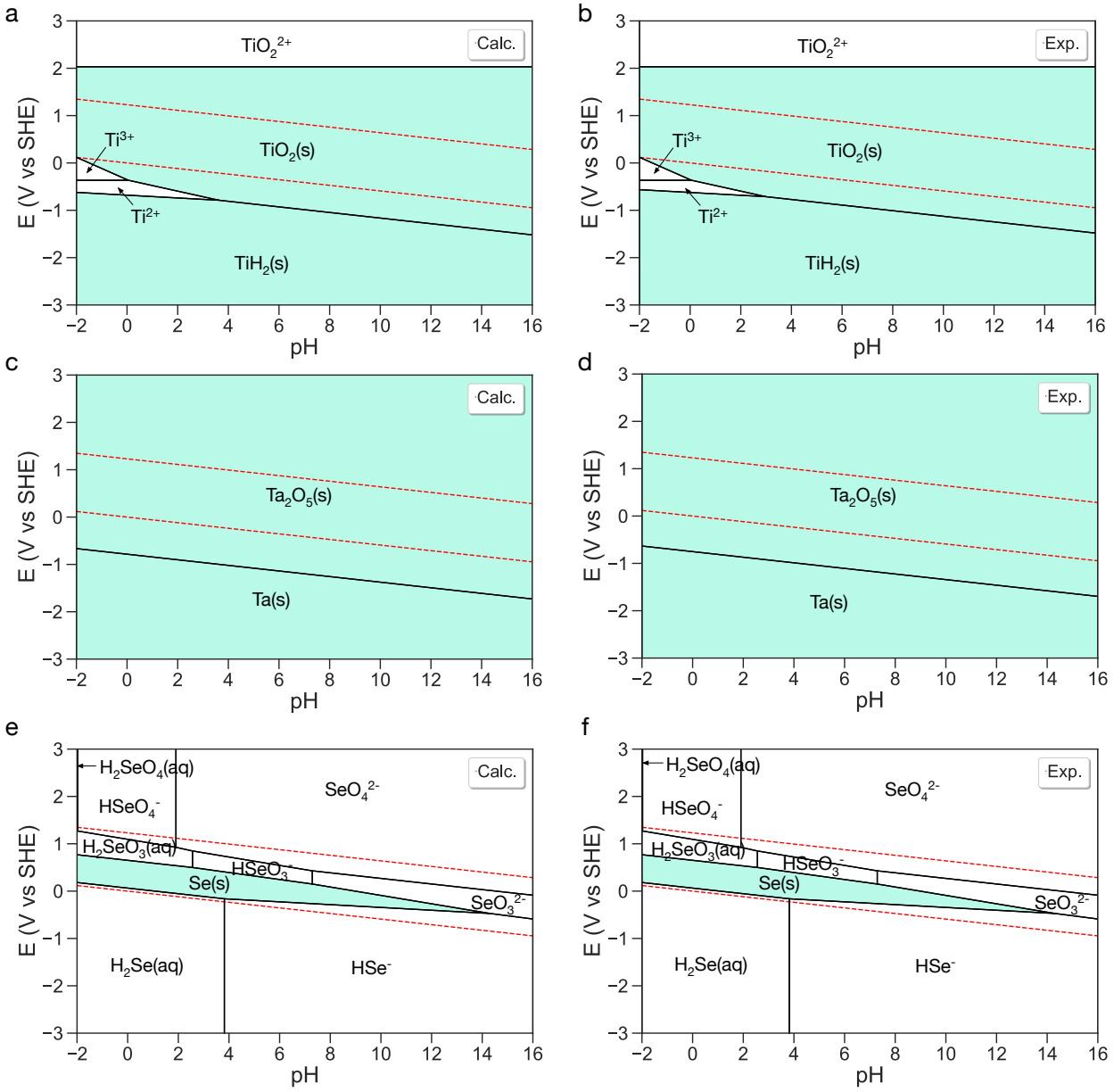

Figure 2: Calculated and experimental Pourbaix diagrams constructed with aqueous ion concentrations 10^{-6} M at 25°C. (a-b) Ti, (c-d) Ta, (e-f) Se. Regions with solid are shaded in Lake blue. The water stability window is shown in red dashed line.

all TM oxides and (oxy)hydroxides in the studied composition space from the MP, we only consider their ferromagnetic configurations in this work. Overall, the calculated Pourbaix diagrams using the SCAN+U functional show better agreement with the experimental diagrams than MP PBE results (Figure 3 and Figure S6). A detailed discussion of each 3*d* metal Pourbaix diagram is presented.

Mn. In Figure 3a, the stability region of $Mn(OH)_2$ is slightly broader than that in the experimental diagram (Figure 3b), resulting in the absence of $Mn(OH)^+$. In the complete Pourbaix diagram (Figure S7a), MnOOH appears in the stability regions of Mn_2O_3 and MnO_2, which is in line with the experimental observations[30] that MnOOH is synthesized at low temperature ($<170°C$) around pH = 11 and transforms to Mn_2O_3 and MnO_2 at high temperature.

Fe. In Figure 3c, the solid and aqueous ions regions are well predicted by our method, compared to the experimental diagram, shown in Figure 3c. In the complete Pourbaix diagram (Figure S7b), FeOOH shows up in the Fe_2O_3 stability region. In experiment, FeOOH is found at low temperature and transforms to Fe_2O_3 after thermal treatment.[31,32] Moreover, high-valence iron oxides (FeO_3, Fe_4O_{13}) and iron hydrides are found to be stable under extremely oxidative and reductive environments, respectively.

Co. Another possible reason for the difference in the stability regions of Co_3O_4 and Co_2O_3 between computation (Figure 3e) and experiment (Figure 3f) is the large uncertainty of experimental Gibbs free formation energy (ΔG_f^{exp}) of Co_3O_4. The reported ΔG_f^{exp} for Co_3O_4 varies by $\sim$1.0 eV/fu. (Table S2) Herein, we use the Pourbaix's atlas data[21] for experimental diagram because it is the most comprehensive. Lowering ΔG_f^{exp} of Co_3O_4 used in this work to other reported values in experiment considerably enlarges its stability region in the experimental diagram. In the complete Pourbaix diagram (Figure S7c), CoOOH is absent in the stability regions of Co_2O_3 and CoO_2 likely due to the influence magnetic configurations.[28,29] The MP PBE results (Figure S6c) has large deviations from the experimental diagram, which is likely because of the inaccurate chemical potential of $HCoO^{2-}$ used. (See Table S2)

Ni. Compared to the experimental Pourbaix diagram (Figure 3h), the large stability region

of $Ni(OH)_2$ results in the absence of Ni_3O_4 and Ni_2O_3 and $Ni(OH)_3^-$ in the calculated Pourbaix diagram (Figure 3g). Similar to cobalt results, NiOOH is absent in the regions of Ni_2O_3 and NiO_2 in the complete Pourbaix diagram (Figure S7d). We note that NiO and/or $Ni(OH)_2$ was often observed to be stable at pH 5$\sim$15 in experiment.[33,34] This is probably because in practical applications the Ni aqueous ion concentration is much higher than the conventional one (10^{-6} M) used in the Pourbaix diagram generation. The stability regions of solids and aqueous ions predicted by the MP PBE are in excellent agreement with the experiment diagram, except for the absence of nickel (oxy)hydroxides. (Figure S6d) This success is ascribed to the correction between referenced solid and aqueous ions.[2] In fact, without $Ni(OH)_2$, the SCAN-calculated Pourbaix diagram yields similar results as the MP PBE. (Figure S8)

Applications

In this section, we showcase applications of our method in accurately predicting the aqueous stability of catalysts for electrocatalysis. IrO_2 and RuO_2 are the state-of-the-art electrocatalysts for oxygen evolution reaction (OER) in acidic media. The typical OER working conditions in acid are pH = 0 or 1 and potentials of 1.23$-$2.0 V. Singh et al.[35] proposed that the aqueous stability can be quantitatively evaluated by computing the material's Gibbs free energy difference (ΔG_{pbx}) with respect to the stable domains in the Pourbaix diagram as a function of pH and potential. We will use this concept to evaluate the aqueous stability of IrO_2 and RuO_2 at OER working conditions.

Figure 4a-b show the calculated Ir Pourbaix diagram and the Pourbaix decomposition free energy of IrO_2 from the potential 0 to 2.0 V at pH = 0, respectively. We find that at pH = 0, IrO_2 transforms to IrO_3 at the potential of 1.55 V and IrO_3 dissolves to IrO_4^- at the potential of 1.60 V, which is consistent with the experimental observations that IrO_2 dissolves at potentials of 1.50 $\sim$ 1.60 V in OER.[36–38] In experiment, the formation of high-valence iridium oxides, e.g. IrO_3 is commonly regarded as the origin of instability of IrO_2 during OER,.[37,39] Based on the DFT calculated Phase diagram (Figure S9), IrO_3 is predicted to be highly unstable in the SCAN functional with a decomposition energy of 159 meV/atom, whereas it is predicted be stable in the PBE functional.

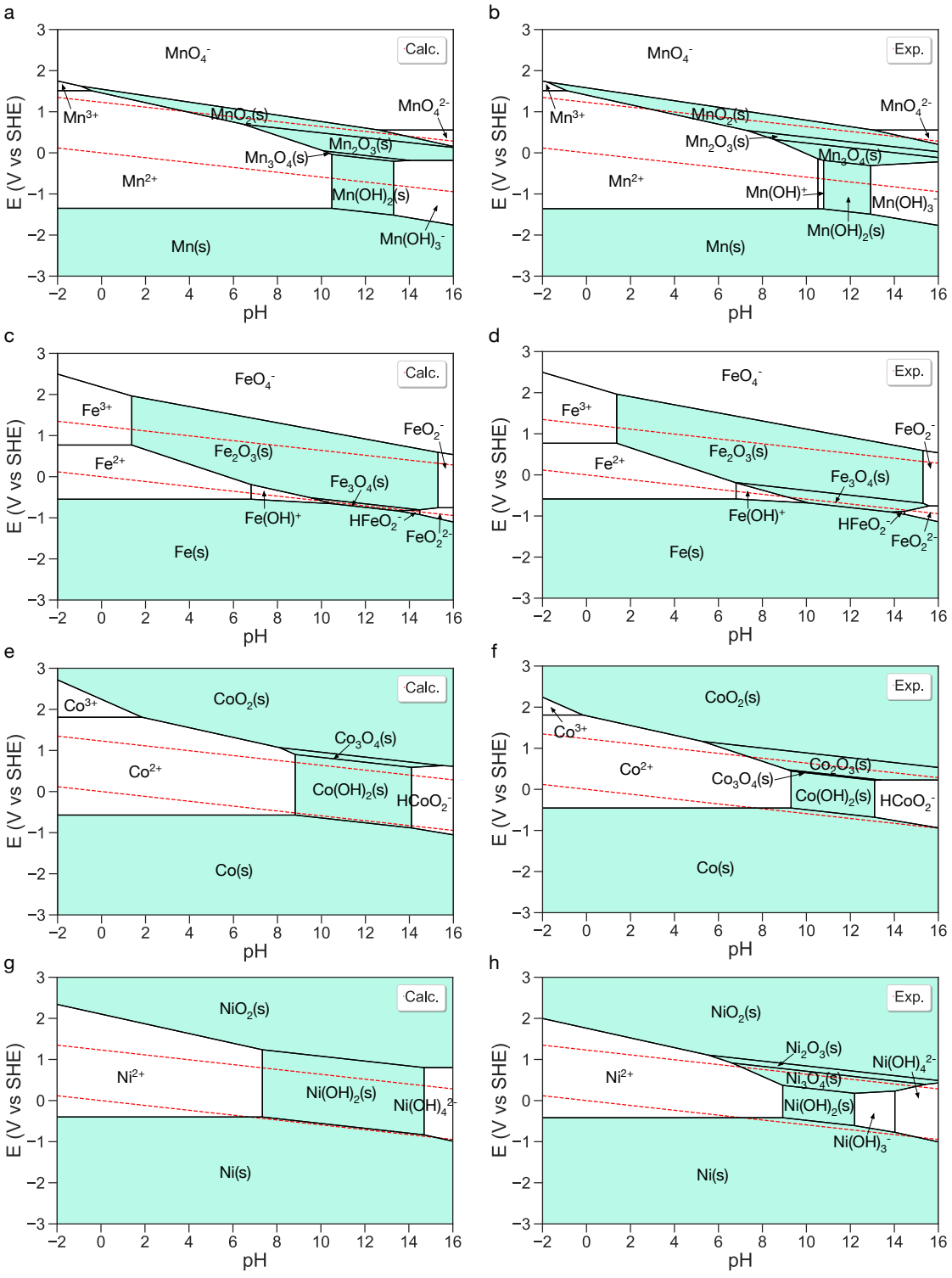

Figure 3: Calculated and experimental transition metal Pourbaix diagrams constructed with aqueous ion concentrations 10^{-6} M at 25°C. (a-b) Mn, (c-d) Fe, (e-f) Co, (g-h) Ni. Regions with solid are shaded in Lake blue. The water stability window is shown in red dashed line.

Considering that IrO_3 is only detected as an intermediate species during OER in experiment,[37,39] we argue that the SCAN functional may give a reasonable phase stability for IrO_3. As shown in Figure S10, the experimental Pourbaix diagram from Pourbaix's atlas[21] severely overestimates the OER stability region of IrO_2 (1.23−1.87 V), while the MP PBE Pourbaix diagram seriously underestimates the stability region of IrO_2 (1.23−1.24 V).

Figure 4a shows the calculated Ru Pourbaix diagram. There are only two solid regions, Ru and RuO_2. In acid, the ruthenium metal is severely corroded, forming Ru^{3+}, and RuO_2 has also a narrow stable region. In experiment, it is generally believed that RuO_2 exists in the form of hydrated oxide, $RuO_2{\cdot}mH_2O$ ($1 \leq m \leq 2$) and could be oxidized or reduced into amorphous Ru_2O_5 and $Ru(OH)_3{\cdot}H_2O$, respectively.[22] Figure 4b shows the calculated Pourbaix decomposition free energy of RuO_2 as a function of potentials at pH = 1. We observe that RuO_2 dissolves to H_2RuO_5 at 1.34 V, which is in line with the experimental results that RuO_2 has a dissolution onset potential of 1.37 V in 0.1 M H_2SO_4.[36] In the MP PBE Pourbaix diagram (Figure S11), RuO_4 is predicted to be stable from 0.92 V to 2.0 V. Experiments indicate that RuO_4 is unstable and readily dissolves in aqueous solution by forming H_2RuO_5.[22]

Discussion

Distinct from the MP method,[2] the chemical potential of liquid water in this work is evaluated by using the gas-phase H_2O at 0.035 bar, since at this pressure the gas-phase H_2O is in equilibrium with liquid water at 298.15 K.[40] Using SCAN, this results in a very accurate $\Delta G_f = -2.461$ eV/fu without any affine corrections. In the MP framework of Pourbaix diagram construction, the chemical potential of hydrogen is corrected such that experimental Gibbs free formation energy of water is exactly replicated by construction. We use a chemical potential of -3.66 eV/atom for hydrogen, equal to half of the Gibbs free energy of hydrogen gas computed using the SCAN functional. We therefore regard the errors in the Gibbs free energy of formation for (oxy)hydroxides and hydrides as those of the SCAN functional itself, instead of from applied hydride corrections (e.g. 0.7∼0.8

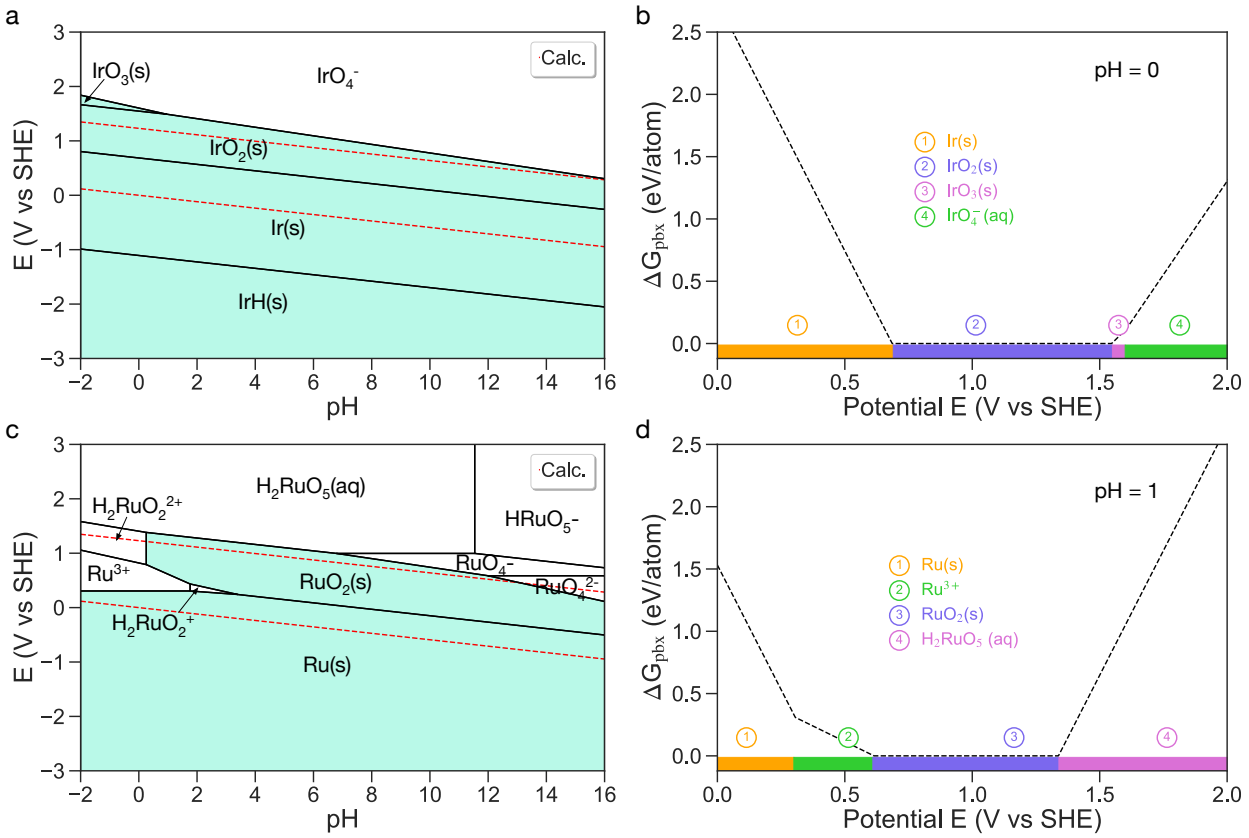

Figure 4: Calculated Pourbaix diagram and Pourbaix decomposition free energy ΔG_{pbx} of OER catalysts in acid. (a)(c) Ir and Ru Pourbaix diagram generated with aqueous ion concentrations 10^{-6} M at 25°C, respectively. (b)(d) Pourbaix decomposition free energy ΔG_{pbx} of IrO_2 and RuO_2 from the potential 0−2.0 V, respectively. The projection of ΔG_{pbx} onto the potential axis highlights the stable species at the corresponding regions.

eV/H_2) in the standard PBE functional.[2,28]

In the reaction energy calculation, we neglect the zero-point energy (E_{ZPE}) and the integrated heat capacity from 0 K to 298.15 K (δH) for both solids and gases by assuming that the differences in these quantities between reactants and products are negligible at room temperature. Previous studies in the literature show that E_{ZPE} and δH of solids and gases are comparable,[28,33,34,41] but we note that estimation of E_{ZPE} and δH is possible, albeit expensive, with phonon or molecular dynamics calculations, and a systematic approach towards these that can further improve our approach merits a study in its own right.

In conclusion, by building on the MP Pourbaix diagram framework, we have developed a simple method to accurately predict the aqueous stability of solids. Benchmark results show that the calculated Pourbaix diagram using the SCAN functional improves the accuracy of predicted aqueous stability in a large number of cases of interest compared to the MP PBE results. We have also demonstrated the applications of this method in quantitatively predicting the dissolution potential of the state-of-the-art OER catalysts in acid, for which both the experimental and/or the MP PBE predictions show large deviations. Our approach enables reliably searching new materials in terms of their aqueous stability for electrochemical applications.

Methods

Density functional theory

The spin-polarized density functional theory (DFT) calculations were performed using the Vienna *ab initio* simulation package (VASP) within the projector-augmented wave method.[42,43] The strongly constrained and appropriately normed (SCAN) functional[8] was used for all structural relaxations and energy calculations. A plane wave energy cutoff of 520 eV was used, and the electronic energy and atomic forces were converged to within 10^{-5} and 0.02 eV/Å, respectively. The Brillouin zone was integrated with a k-point density of at least 1000 per reciprocal atom.[5] We followed the Materials Project selection of transition metal (M = V, Cr, Mn, Fe, Co, Ni, Mo) ox-

ides for Hubbard U corrections.[7,13,44] Note that the U correction for tungsten (W) oxides was not considered in this work due to the poor convergence of SCAN calculations. For simplicity only ferromagnetic configurations were considered for transition metal oxides. All crystal structure manipulations and data analysis were carried out using the Pymatgen software package.[16]

Pourbaix diagram

All the Pourbaix diagrams were constructed using the Materials Project (MP) method developed by Persson[2] as implemented in Pymatgen.[16] In the MP method, the stable domains on the Pourbaix diagram are determined based on the knowledge of all possible equilibrium redox reactions in the chemical composition of interest. In an aqueous medium under a given pH ($-log[\mathrm{H^+}]$) and potential (E), the following redox reaction occurs:

$$[Reactants] + \mathrm{H_2O} \Leftrightarrow [Products] + m\mathrm{H^+} + n\mathrm{e^-} \tag{1}$$

At equilibrium, the Gibbs free energy change (ΔG_{rxn}) of this reaction can be related to E using the Nernst equation:

$$-nFE = \Delta G_{\mathrm{rxn}} = \Delta G^{\mathrm{o}}_{\mathrm{rxn}} + 2.303 \times RT \times log\frac{a_{Reactants}}{a_{Products}} - 2.303 \times RT \times m \times pH \tag{2}$$

where $\Delta G^{\mathrm{o}}_{\mathrm{rxn}}$ is the Gibbs free energy change of the reaction at standard conditions, F is the Faraday constant, R is the gas constant, and T is the temperature. a is the activity coefficient. The most stable species in aqueous solutions can be therefore determined by minimizing (ΔG_{rxn} + nFE) across all possible reactions under certain pH and applied potential.

The chemical potential of a material under standard conditions can be expressed as:

$$\mu^0 = H^0 - TS^0 = E_{DFT} + E_{ZPE} + \delta H - TS^0 \tag{3}$$

where E_{DFT} is the DFT calculated total energy, E_{ZPE} is the zero-point energy, δH is the integrated

heat capacity from 0 K to 298.15 K, TS^0 is the entropy contribution at the standard conditions. For gas phase species, the DFT total energy was evaluated by a molecule in a $15 \times 15 \times 15$ Å box, S^0 data were collected the experimental thermodynamic database.[19] For solid phase species, the entropy contribution was neglected since it was very small compared to the gas species. The E_{ZPE} and δH for both solid and gas species were neglected by assuming that these energies have similar contributions between species and therefore cancel out in reaction energies.

The chemical potentials of aqueous ionic species were obtained from experimental data with a correction of the referenced solid phase energy difference between DFT calculations and experiments. ($\mu_{solid-solid}$)

$$\mu^0_{ion} = \mu^0_{ion,exp} + \Delta\mu_{solid-solid} \tag{4}$$

The experimental formation Gibbs free energy of referenced solid and aqueous ions were collected from Ref.[20–22]

Data availability

All data necessary to support the findings of this study is available in the supplementary information. Further data and codes can be made available from Z.W.

Acknowledgements

This work was supported by Toyota Research Institute.

Contributions

Z.W and J.K.N designed the study. Z.W. performed the calculations, developed the code, analyzed the data and wrote the manuscript. X.G contributed to the code development and data analysis. J.M contributed to data analysis. All authors discussed the results and commented on the manuscript.

Competing interests

The authors declare no competing interests.

References

(1) Hansen, H. A.; Rossmeisl, J.; Nørskov, J. K. Surface Pourbaix diagrams and oxygen reduction activity of Pt, Ag and Ni(111) surfaces studied by DFT. *Physical Chemistry Chemical Physics* **2008**, *10*, 3722–3730.

(2) Persson, K. A.; Waldwick, B.; Lazic, P.; Ceder, G. Prediction of solid-aqueous equilibria: Scheme to combine first-principles calculations of solids with experimental aqueous states. *Physical Review B - Condensed Matter and Materials Physics* **2012**, *85*, 1–12.

(3) Montoya, J. H.; Garcia-Mota, M.; Nørskov, J. K.; Vojvodic, A. Theoretical evaluation of the surface electrochemistry of perovskites with promising photon absorption properties for solar water splitting. *Physical Chemistry Chemical Physics* **2015**, *17*, 2634–2640.

(4) Singh, A. K.; Montoya, J. H.; Gregoire, J. M.; Persson, K. A. Robust and synthesizable photocatalysts for CO_2 reduction: a data-driven materials discovery. *Nature Communications* **2019**, *10*, 443.

(5) Jain, A.; Hautier, G.; Ong, S. P.; Moore, C. J.; Fischer, C. C.; Persson, K. A.; Ceder, G. Formation enthalpies by mixing GGA and GGA+U calculations. *Physical Review B* **2011**, *84*, 45115.

(6) National Center for Biotechnology Information, Selenium dioxide, CID=24007. `https://pubchem.ncbi.nlm.nih.gov/compound/Selenium-dioxide(accessedonJune11, 2020).`

(7) Wang, L.; Maxisch, T.; Ceder, G. Oxidation energies of transition metal oxides within the GGA+U framework. *Physical Review B* **2006**, *73*, 195107.

(8) Sun, J.; Ruzsinszky, A.; Perdew, J. Strongly Constrained and Appropriately Normed Semilocal Density Functional. *Physical Review Letters* **2015**, *115*, 036402.

(9) Sun, J.; Remsing, R. C.; Zhang, Y.; Sun, Z.; Ruzsinszky, A.; Peng, H.; Yang, Z.; Paul, A.; Waghmare, U.; Wu, X.; Klein, M. L.; Perdew, J. P. Accurate first-principles structures and energies of diversely bonded systems from an efficient density functional. *Nature Chemistry* **2016**, *8*, 831–836.

(10) Kitchaev, D. A.; Peng, H.; Liu, Y.; Sun, J.; Perdew, J. P.; Ceder, G. Energetics of MnO2 polymorphs in density functional theory. *Physical Review B* **2016**, *93*, 045132.

(11) Zhang, Y.; Kitchaev, D. A.; Yang, J.; Chen, T.; Dacek, S. T.; Sarmiento-Pérez, R. A.; Marques, M. A.; Peng, H.; Ceder, G.; Perdew, J. P.; Sun, J. Efficient first-principles prediction of solid stability: Towards chemical accuracy. *npj Computational Materials* **2018**, *4*.

(12) Perdew, J. P.; Zunger, A. Self-interaction correction to density-functional approximations for many-electron systems. *Physical Review B* **1981**, *23*, 5048–5079.

(13) Jain, A.; Ong, S. P.; Hautier, G.; Chen, W.; Richards, W. D.; Dacek, S.; Cholia, S.; Gunter, D.; Skinner, D.; Ceder, G.; Persson, K. A. Commentary: The materials project: A materials genome approach to accelerating materials innovation. *APL Materials* **2013**, *1*, 011002.

(14) Pople, J. A.; Head-Gordon, M.; Fox, D. J.; Raghavachari, K.; Curtiss, L. A. Gaussian-1 theory: A general procedure for prediction of molecular energies. *The Journal of Chemical Physics* **1989**, *90*, 5622–5629.

(15) Zhang, Y.; Yang, W. Comment on "generalized gradient approximation made simple". *Physical Review Letters* **1998**, *80*, 890.

(16) Ong, S. P.; Richards, W. D.; Jain, A.; Hautier, G.; Kocher, M.; Cholia, S.; Gunter, D.; Chevrier, V. L.; Persson, K. A.; Ceder, G. Python Materials Genomics (pymatgen): A robust, open-source python library for materials analysis. *Computational Materials Science* **2013**, *68*, 314–319.

(17) Ong, S. P.; Cholia, S.; Jain, A.; Brafman, M.; Gunter, D.; Ceder, G.; Persson, K. A. The Materials Application Programming Interface (API): A simple, flexible and efficient API for materials data based on REpresentational State Transfer (REST) principles. *Computational Materials Science* **2015**, *97*, 209–215.

(18) O. Kubaschewski, C. B. Alcock, and P. J. Spencer, *Materials thermochemistry*, 6th ed.; Pergamon Press, 1993.

(19) P.J. Linstrom and W.G. Mallard, E. *NIST Chemistry WebBook, NIST Standard Reference Database Number 69*; National Institute of Standards and Technology, Gaithersburg MD, 20899, https://doi.org/10.18434/T4D303, (retrieved May 18, 2020), 2020.

(20) Wagman, D. D.; Evans, W. H.; Halow, I.; Parker, V. B.; Bailey, S. M.; Schumm, R. H.; (U.S.), I. f. B. S.; of Standards, U. S. N. B.; of Commerce, U. S. D. *Selected Values of Chemical Thermodynamic Properties*; NBS technical note; United States Department of Commerce, National Bureau of Standards, 1966.

(21) Pourbaix, M. *Atlas of Electrochemical Equilibria in Aqueous Solutions.*, 2nd ed.; National Association of Corrosion Engineers, 1974: NACE.

(22) Rard, J. A. Chemistry and thermodynamics of ruthenium and some of its inorganic compounds and aqueous species. *Chemical Reviews* **1985**, *85*, 1–39.

(23) Pley, M.; Wickleder, M. S. Two crystalline modifications of RuO_4. *Journal of Solid State Chemistry* **2005**, *178*, 3206–3209.

(24) Juodkazis, K.; Juodkazytė, J.; Tabuchi, Y.; Juodkazis, S.; Matsuo, S.; Misawa, H. Deposition of platinum and irridium on Ti surface using femtosecond laser and electrochemical activation. *Lith. J. Phys.* **2003**, *43*, 209–216.

(25) Hwang, H.; Lim, D.; Kim, T.; Lee, D.; Shim, S. E.; Baeck, S.-H. Electro-Catalytic Activity of RuO_2–IrO_2–Ta_2O_5 Mixed Metal Oxide Prepared by Spray Thermal Decomposition for

Alkaline Water Electrolysis. *Journal of Nanoscience and Nanotechnology* **2016**, *16*, 4405–4410.

(26) Xiao, W.; Huang, X.; Song, W.; Yang, Y.; Herng, T. S.; Xue, J. M.; Feng, Y. P.; Ding, J. High catalytic activity of oxygen-induced (200) surface of Ta_2O_5 nanolayer towards durable oxygen evolution reaction. *Nano Energy* **2016**, *25*, 60–67.

(27) Deblonde, G. J.; Chagnes, A.; Bélair, S.; Cote, G. Solubility of niobium(V) and tantalum(V) under mild alkaline conditions. *Hydrometallurgy* **2015**, *156*, 99–106.

(28) Zeng, Z.; Chan, M. K.; Zhao, Z. J.; Kubal, J.; Fan, D.; Greeley, J. Towards First Principles-Based Prediction of Highly Accurate Electrochemical Pourbaix Diagrams. *Journal of Physical Chemistry C* **2015**, *119*, 18177–18187.

(29) Long, O. Y.; Sai Gautam, G.; Carter, E. A. Evaluating optimal U for 3d transition-metal oxides within the SCAN+U framework Olivia. *Physical Review Materials* **2020**, *4*, 045401.

(30) Sharma, P. K.; Whittingham, M. S. The role of tetraethyl ammonium hydroxide on the phase determination and electrical properties of γ-MnOOH synthesized by hydrothermal. *Materials Letters* **2001**, *48*, 319–323.

(31) Musić, S.; Krehula, S.; Popović, S. Thermal decomposition of β-FeOOH. *Materials Letters* **2004**, *58*, 444–448.

(32) Ristić, M.; Musić, S.; Godec, M. Properties of γ-FeOOH, α-FeOOH and α-Fe_2O_3 particles precipitated by hydrolysis of Fe^{3+} ions in perchlorate containing aqueous solutions. *Journal of Alloys and Compounds* **2006**, *417*, 292–299.

(33) Huang, L. F.; Hutchison, M. J.; Santucci, R. J.; Scully, J. R.; Rondinelli, J. M. Improved Electrochemical Phase Diagrams from Theory and Experiment: The Ni-Water System and Its Complex Compounds. *Journal of Physical Chemistry C* **2017**, *121*, 9782–9789.

(34) Huang, L.-F.; Rondinelli, J. M. Reliable electrochemical phase diagrams of magnetic transition metals and related compounds from high-throughput *ab initio* calculations. *npj Materials Degradation* **2019**, *3*.

(35) Singh, A. K.; Zhou, L.; Shinde, A.; Suram, S. K.; Montoya, J. H.; Winston, D.; Gregoire, J. M.; Persson, K. A. Electrochemical Stability of Metastable Materials. *Chemistry of Materials* **2017**, *29*, 10159–10167.

(36) Cherevko, S.; Geiger, S.; Kasian, O.; Kulyk, N.; Grote, J.-P.; Savan, A.; Shrestha, B. R.; Merzlikin, S.; Breitbach, B.; Ludwig, A.; Mayrhofer, K. J. Oxygen and hydrogen evolution reactions on Ru, RuO_2 , Ir, and IrO_2 thin film electrodes in acidic and alkaline electrolytes: A comparative study on activity and stability. *Catalysis Today* **2016**, *262*, 170–180.

(37) Kasian, O.; Grote, J.-P.; Geiger, S.; Cherevko, S.; Mayrhofer, K. J. J. The Common Intermediates of Oxygen Evolution and Dissolution Reactions during Water Electrolysis on Iridium. *Angewandte Chemie International Edition* **2018**, *57*, 2488–2491.

(38) Geiger, S.; Kasian, O.; Ledendecker, M.; Pizzutilo, E.; Mingers, A. M.; Fu, W. T.; Diaz-Morales, O.; Li, Z.; Oellers, T.; Fruchter, L.; Ludwig, A.; Mayrhofer, K. J.; Koper, M. T.; Cherevko, S. The stability number as a metric for electrocatalyst stability benchmarking. *Nature Catalysis* **2018**, *1*, 508–515.

(39) Pearce, P. E.; Yang, C.; Iadecola, A.; Rodriguez-Carvajal, J.; Rousse, G.; Dedryvère, R.; Abakumov, A. M.; Giaume, D.; Deschamps, M.; Tarascon, J. M.; Grimaud, A. Revealing the Reactivity of the Iridium Trioxide Intermediate for the Oxygen Evolution Reaction in Acidic Media. *Chemistry of Materials* **2019**, *31*, 5845–5855.

(40) Nørskov, J. K.; Rossmeisl, J.; Logadottir, A.; Lindqvist, L.; Kitchin, J. R.; Bligaard, T.; Jónsson, H. Origin of the overpotential for oxygen reduction at a fuel-cell cathode. *Journal of Physical Chemistry B* **2004**, *108*, 17886–17892.

(41) Lany, S. Semiconductor thermochemistry in density functional calculations. *Physical Review B - Condensed Matter and Materials Physics* **2008**, *78*, 1–8.

(42) Kresse, G.; Furthmüller, J. Efficient iterative schemes for *ab initio* total-energy calculations using a plane-wave basis set. *Physical Review B* **1996**, *54*, 11169–11186.

(43) Blöchl, P. E. Projector augmented-wave method. *Physical Review B* **1994**, *50*, 17953–17979.

(44) Dudarev, S. L.; Botton, G. A.; Savrasov, S. Y.; Humphreys, C. J.; Sutton, A. P. Electron-energy-loss spectra and the structural stability of nickel oxide: An LSDA+U study. *Physical Review B* **1998**, *57*, 1505–1509.

SUPPORTING INFORMATION

Predicting Aqueous Stability of Solid with Computed Pourbaix Diagram using SCAN Functional

Zhenbin Wang,[†] Xingyu Guo,[‡] Joseph Montoya,[¶] and Jens K. Nørskov[*,†]

†*CatTheory, Department of Physics, Technical University of Denmark, 2800 Kongens Lyngby, Denmark*

‡*Materials Science and Engineering Program, University of California San Diego, 9500 Gilman Dr, La Jolla, CA 92093, USA*

¶*Toyota Research Institute, Los Altos, CA 94022, USA*

E-mail: jkno@dtu.dk

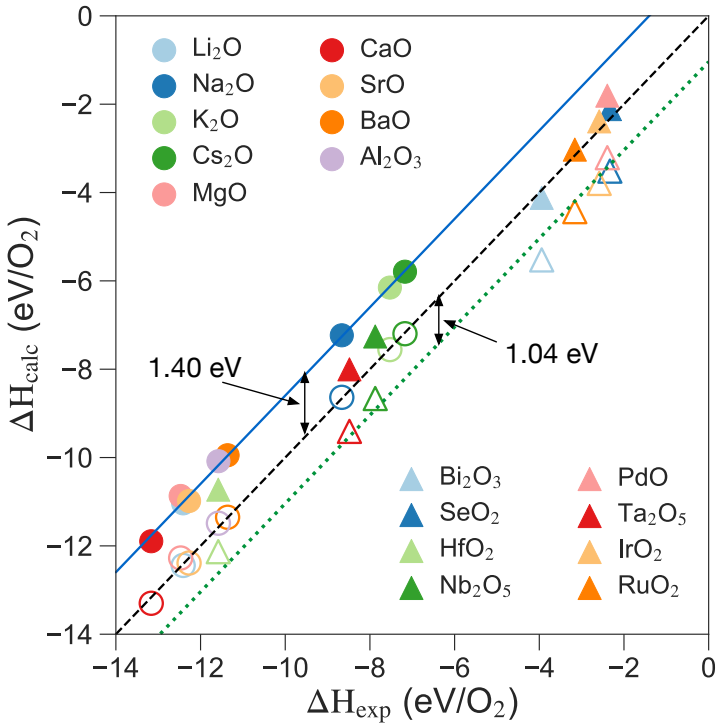

Figure S1: Calculated formation enthalpies of representative oxides as a function of the experimental enthalpies. The solid and open symbols refer to data of raw PBE and PBE with O_2 correction, respectively. The solid blue line gives the fitted O_2 correction (1.40 eV/fu) adopted in the Materials Project (MP) for oxide compounds. The dotted line is the best fit (1.04 eV/fu) for the eight representative oxides deviating from the experimental values after applying the MP O_2 correction. All PBE data were retrieved from the Materials Project [1–3] and the experimental formation enthalpies were obtained from 4–6

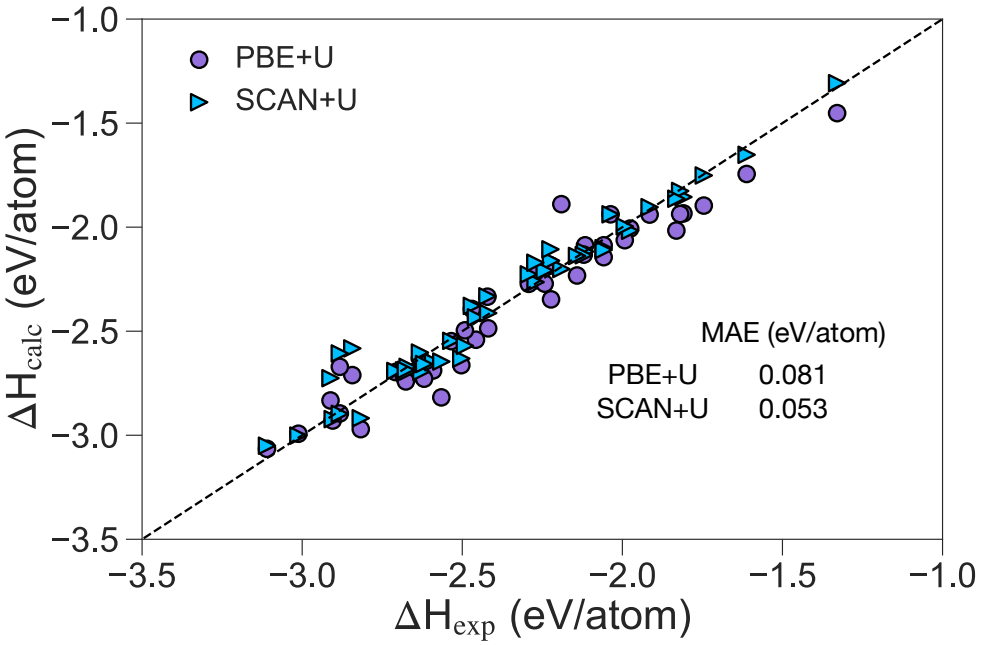

Figure S2: Calculated formation enthalpies of 47 ternary transition metal oxides as a function of experiment formation enthalpies. The PBE+U data were retrieved from the Materials Project.[1–3] and the experimental enthalpies were obtained from Ref 4, 5, 7. The raw data for this plot are provided in Table S4.

Table S1: Calibrated Hubbard U parameters (eV) and the corresponding energy adjustment (ΔE_M, M=metal, eV) when mixing the SCAN and SCAN+U energies in the formation enthalpy calculation for transition metal oxides. Detailed fitting procedures were described in Ref 7.

Element	Hubbard U	ΔE_M
V	0.66	0
Cr	0.22	0.552
Mn	2.93	-0.941
Fe	2.86	-1.116
Co	2.86	-1.118
Ni	2.43	-0.641
Mo	2.05	-1.624

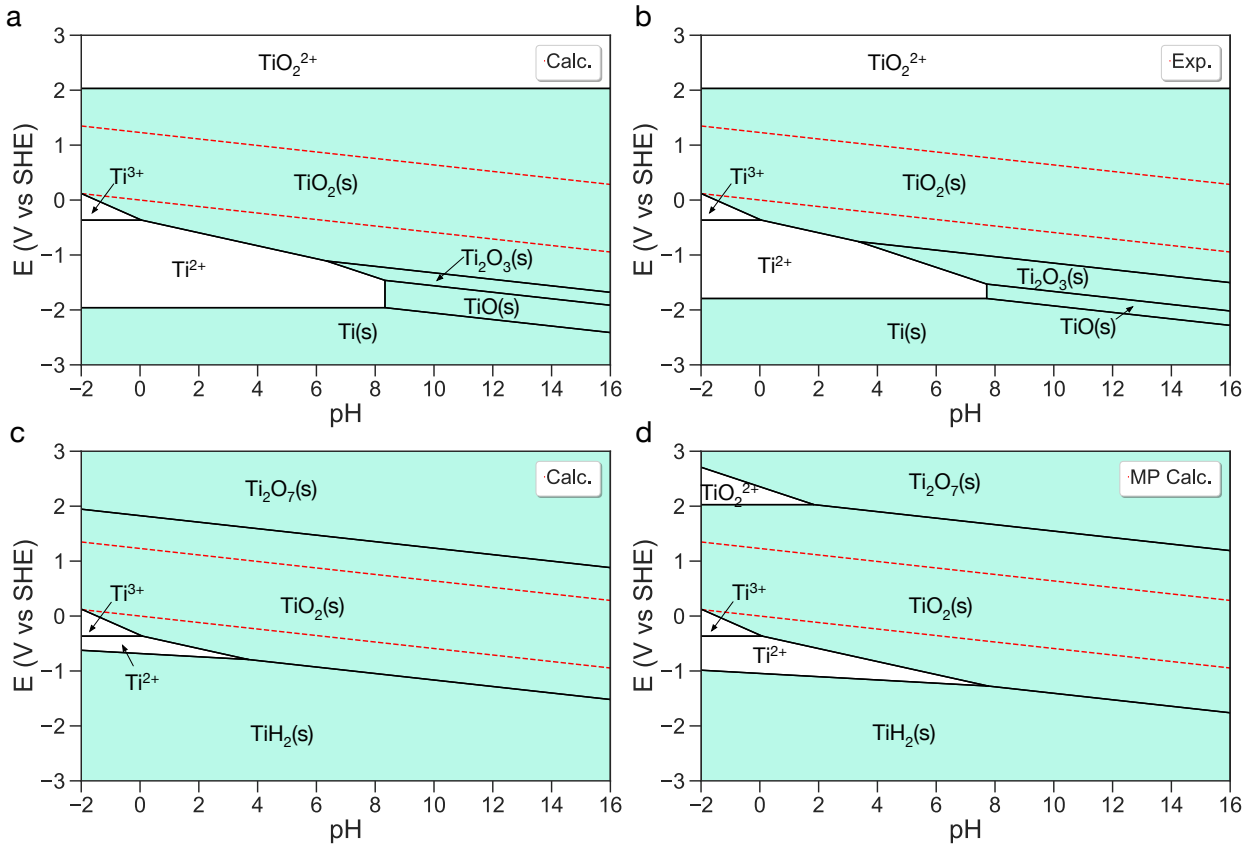

Figure S3: Ti Pourbaix diagrams generated with aqueous ion concentrations of 10^{-6} M at 25°C. (a) SCAN-calculated and (b) experimental Pourbaix diagram generated without TiH_2. (c) SCAN-calculated Pourbaix diagrams by including all materials in the Ti-O-H composition space from the Materials Project.[1–3] (d) The Materials Project PBE-calculated Pourbaix diagram.[1–3] Regions with solid are shaded in Lake blue. The water stability window is shown in red dashed line.

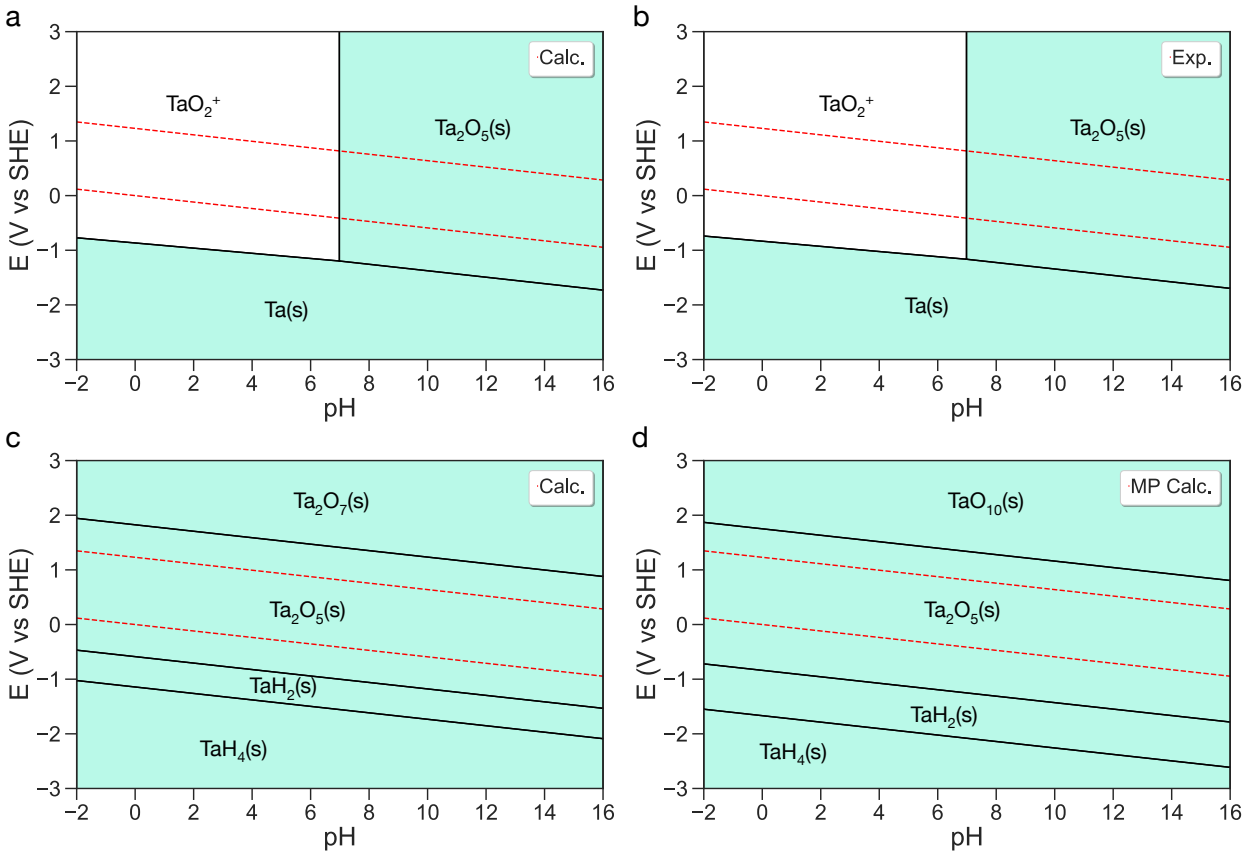

Figure S4: Ta Pourbaix diagrams generated with aqueous ion concentration of 10^{-6} M at 25°C. (a) SCAN-calculated and (b) experimental Ta Pourbaix diagram without TaO_2^{2+}. (c) SCAN-calculated Ta Pourbaix diagram by including all materials in the Ta-O-H composition space from the Materials Project (MP).[1–3] (d) The MP PBE-calculated Pourbaix diagram.[1–3] Regions with solid are shaded in Lake blue. The water stability window is shown in red dashed line.

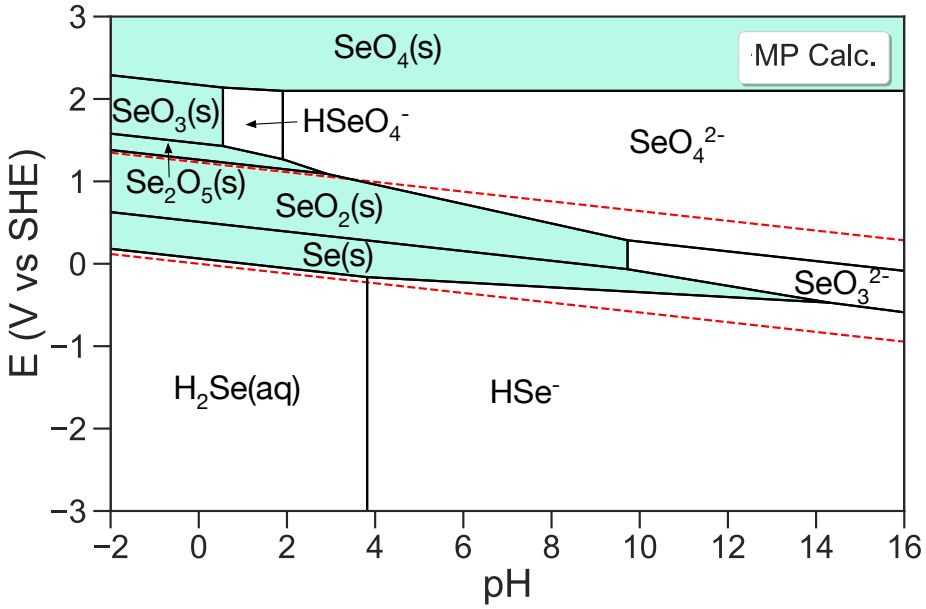

Figure S5: The Materials Project PBE calculated Se Pourbaix diagram with aqueous ion concentration of 10^{-6} M at 25°C. Regions with solid are shaded in Lake blue. The water stability window is shown in red dashed line. All data were retrieved from the Materials Project. [1–3]

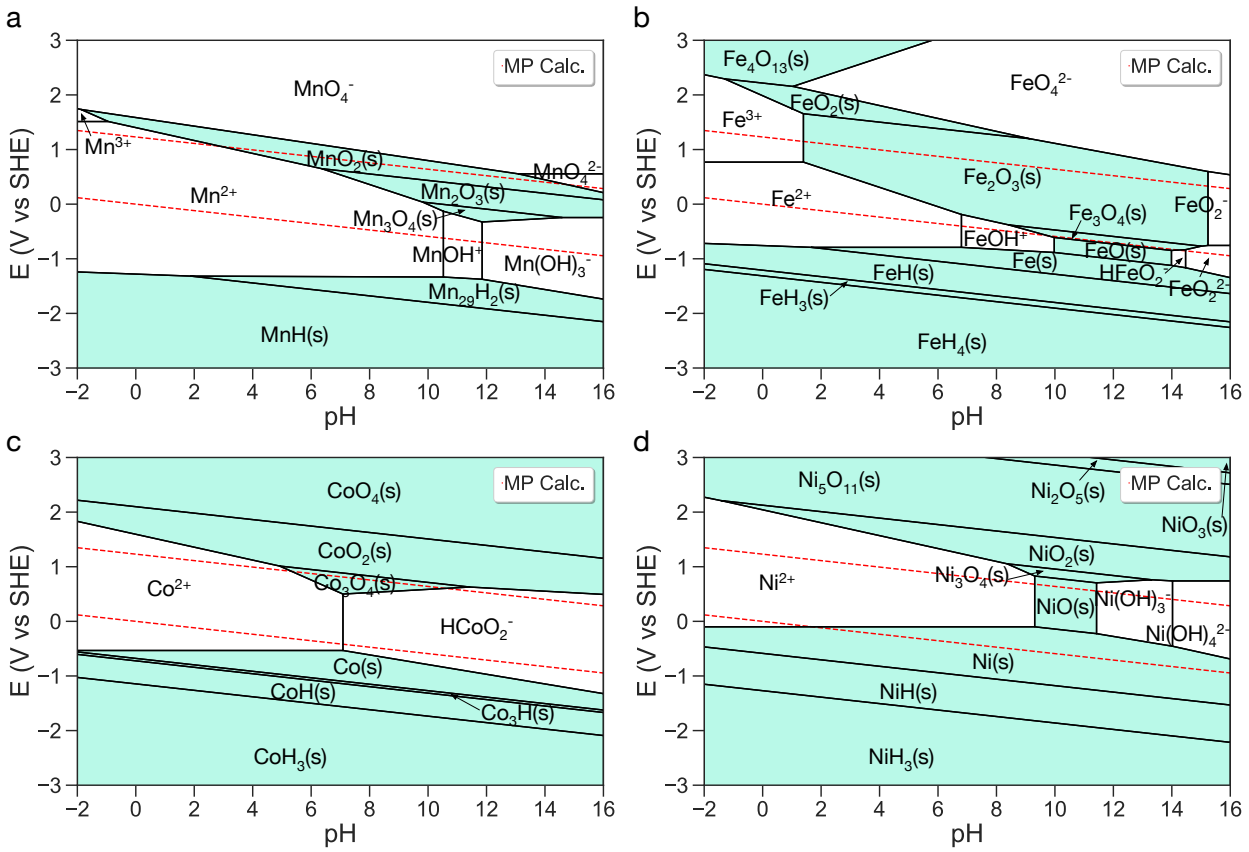

Figure S6: The Materials Project PBE+U calculated (a) Mn, (b) Fe, (c) Co, (d) Ni Pourbaix diagrams with aqueous ion concentration of 10^{-6} M at 25°C. Regions with solid are shaded in Lake blue. The water stability window is shown in red dashed line. All data were retrieved from the Materials Project.[1–3]

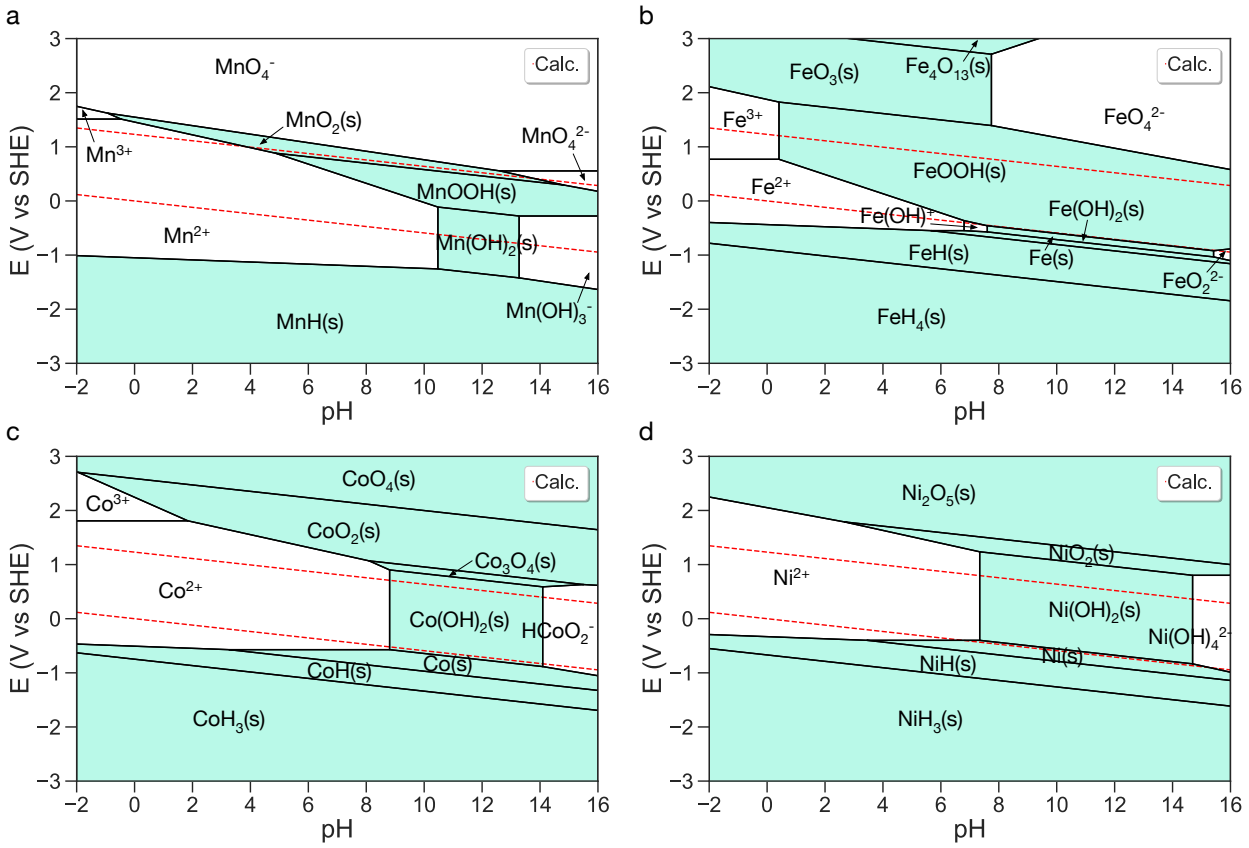

Figure S7: Calculated (a) Mn, (b) Fe, (c) Co, (d) Ni Pourbaix diagrams with aqueous ion concentration of 10^{-6} M at 25°C. These Pourbaix diagram were constructed by computing all materials in the M-O-H (M = Mn/Fe/Co/Ni) composition space from the Materials Project using the SCAN(+U) functional. Regions with solid are shaded in Lake blue. The water stability window is shown in red dashed line.

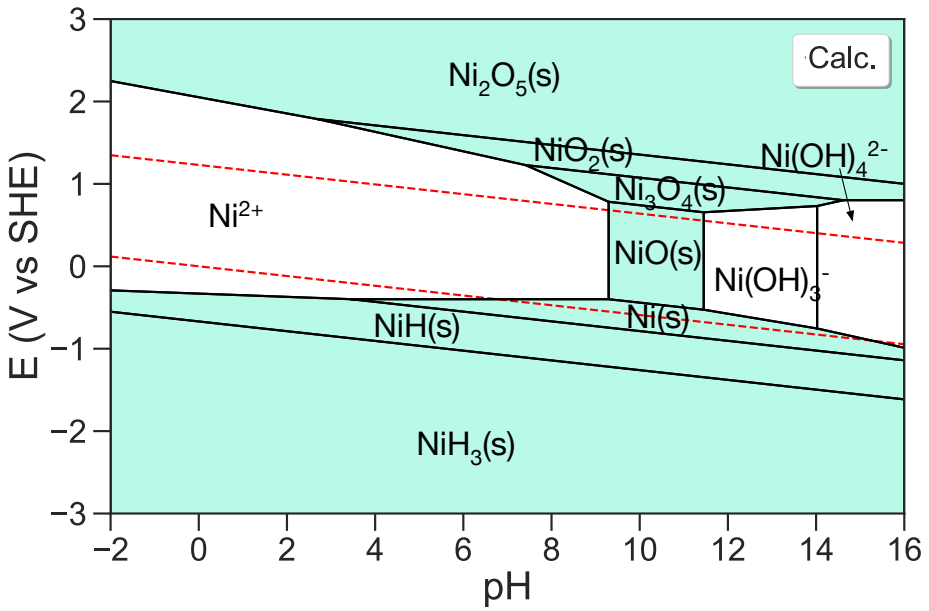

Figure S8: SCAN(+U)-calculated Ni Pourbaix diagrams using aqueous ion concentration of 10^{-6} M at 25°C. Regions with solid are shaded in Lake blue. The water stability window is shown in red dashed line.

Table S2: The experimental formation Gibbs free energy (eV/fu) of Co solids and aqueous ions. Pourbaix's data were used in this work for experimental Poubaix diagram generation. Wagman's data were used by the Materials Project.

Species	Pourbaix[8]	Wagman[6]	Barin[9]
Co^{2+}	-0.555	-0.564	
Co^{3+}	1.253	1.386	-
$HCoO_2^-$	-3.598	-4.224	-
$Co(OH)_2$(aq)	-	-3.825	-
CoO	-2.125	-2.220	-2.220
Co_3O_4	-7.278	-8.022	-8.238
Co_2O_3(hydr)	-4.992	-	-
CoO_2	-2.248	-	-
$Co(OH)_2$	-4.727	-4.748	-4.797
$Co(OH)_3$	-6.184	-	-

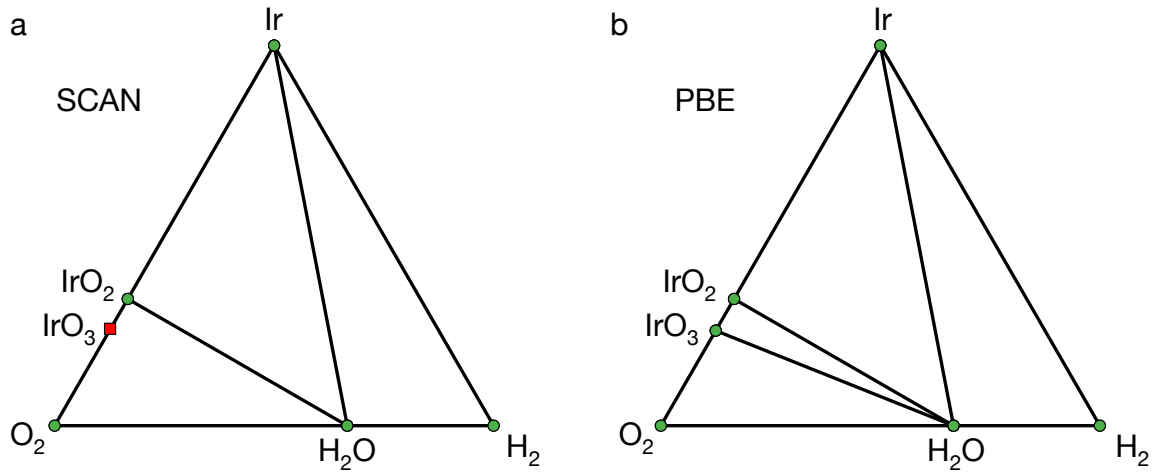

Figure S9: DFT calculated phase diagram in the Ir-O-H composition spaces using the (a) SCAN and (b) PBE functionals. The green solid circle and the red solid square labels stable and metastable phases, respectively. The PBE data were retrieved from the Materials Project.[1–3]

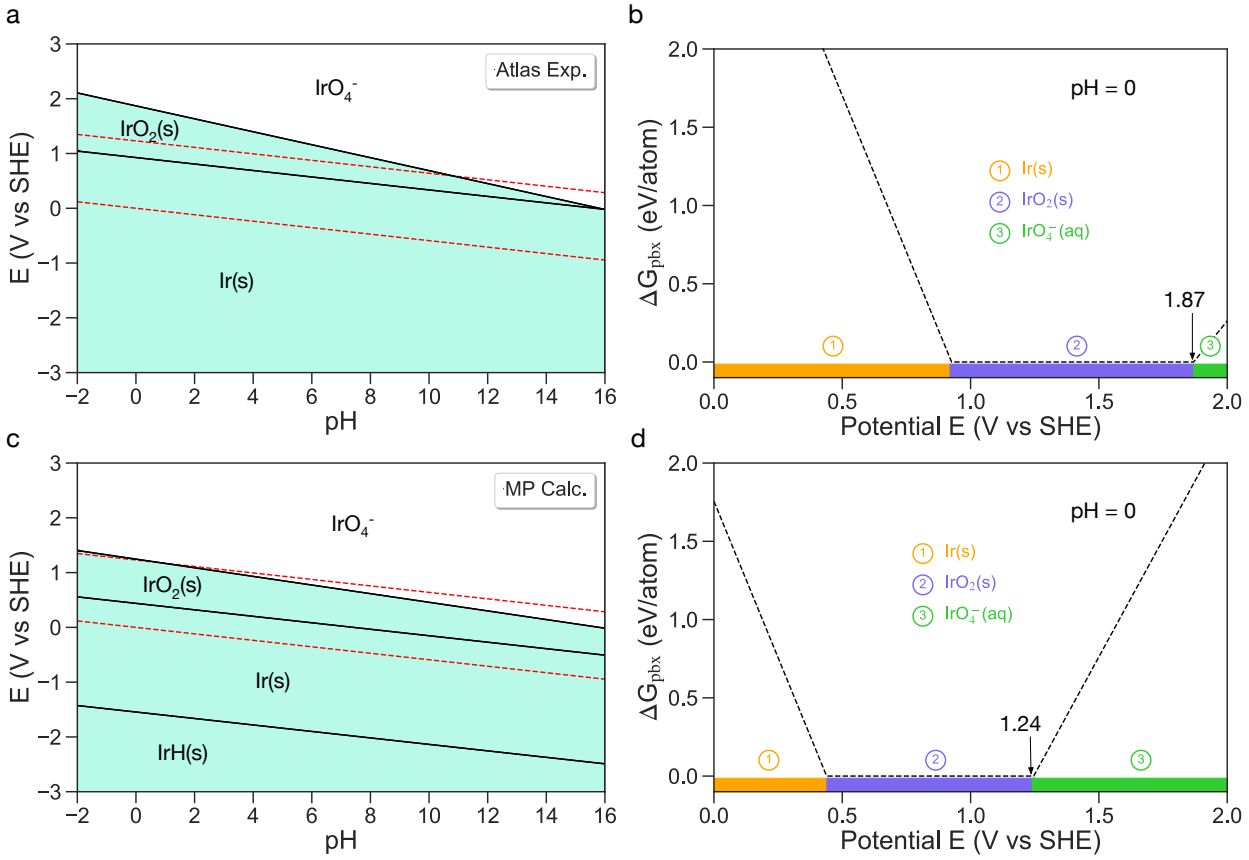

Figure S10: (a) Experimental and (c) the Materials Project (MP) PBE calculated Ir Pourbaix diagrams generated using aqueous ion concentration of 10^{-6} M at 25°C. Regions with solid are shaded in Lake blue. The water stability window is shown in red dashed line. (b-d) Computed Pourbaix decomposition free energy (ΔG_{pbx}) of IrO_2 in experimental and the MP PBE diagrams from the potential 0−2.0 V at pH = 0, respectively. The projection of ΔG_{pbx} onto the potential axis highlights the stable species at the corresponding regions. The labels with arrow show the onset dissolution potential of IrO_2 under OER conditions. The experimental and the MP PBE data were retrieved from Ref 8 and the Materials Project,[1–3] respectively.

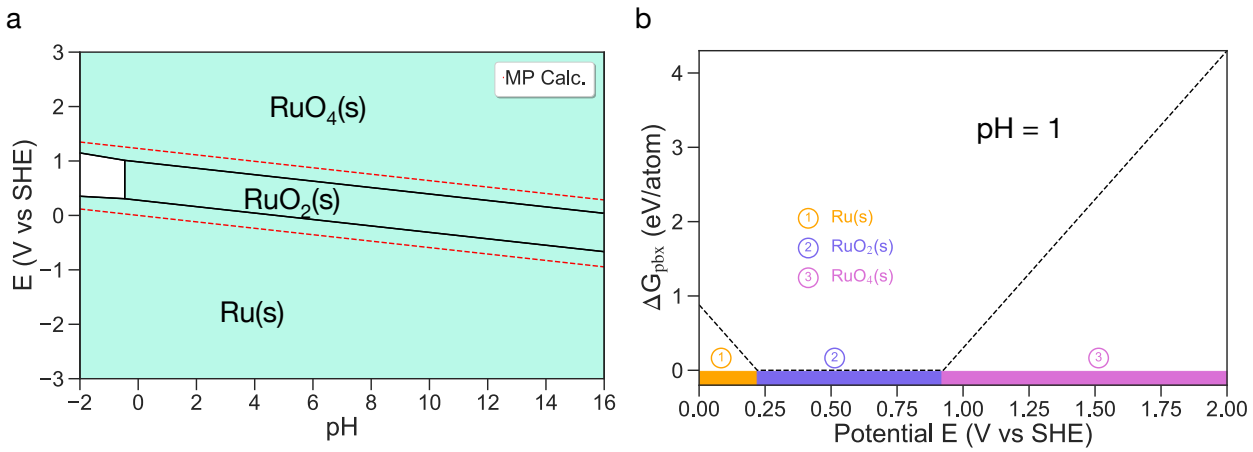

Figure S11: (a) The Materials Project (MP) PBE calculated Ru Pourbaix diagrams generated using aqueous ion concentration of 10^{-6} M at 25°C. Regions with solid are shaded in Lake blue. The water stability window is shown in red dashed line.. (b) Computed Pourbaix decomposition free energy (ΔG_{pbx}) of RuO_2 in (a) from the potential 0−2.0 V at pH = 1. The projection of ΔG_{pbx} onto the potential axis highlights the stable species at the corresponding regions. All data were retrieved from the Materials Project.[1–3]

Table S3: Calculated and experimental formation enthalpies (eV/atom) of 114 binary oxides. ΔH_{SCAN} and ΔH_{SCAN+U} are data calculated using the SCAN functional and the SCAN+U functional for transition metal oxides, respectively. ΔH_{MP} refers to the PBE(+U) data retrieved from the Materials Project.[1–3] The experimental data were obtained from Ref 4, 5.

Formula	ΔH_{exp}	ΔH_{MP}	ΔH_{SCAN}	ΔH_{SCAN+U}	Formula	ΔH_{exp}	ΔH_{MP}	ΔH_{SCAN}	ΔH_{SCAN+U}
Ag_2O	-0.107	-0.334	-0.165		Nb_2O_5	-2.812	-3.094	-2.789	
Ag_2O_3	0.07	-0.377	-0.14		NbO	-2.175	-1.476	-2.154	
AgO	-0.063	-0.46	-0.217		NbO_2	-2.747	-2.917	-2.708	
Al_2O_3	-3.473	-3.446	-3.436		Nd_2O_3	-3.748	-3.803	-3.721	
As_2O_3	-1.38	-1.649	-1.336		NiO	-1.242	-0.937	-1.27	-1.238
As_2O_5	-1.362	-1.584	-1.261		OsO_2	-1.018	-1.367	-1.003	
Au_2O_3	-0.007	-0.471	-0.255		OsO_4	-0.816	-1.553	-0.975	
B_2O_3	-2.64	-2.816	-2.622		P_2O_5	-2.228	-2.461	-2.212	
BaO	-2.84	-2.838	-2.761		Pb_3O_4	-1.064	-1.471	-1.113	
BaO_2	-2.191	-2.173	-2.122		PbO	-1.137	-1.491	-1.191	
BeO	-3.158	-3.125	-3.087		PbO_2	-0.948	-1.318	-0.921	
Bi_2O_3	-1.183	-1.658	-1.226		PdO	-0.599	-0.803	-0.687	
CaO	-3.291	-3.325	-3.275		Pr_2O_3	-3.751	-3.755	-3.674	
CdO	-1.339	-1.386	-1.263		Pt_3O_4	-0.4	-0.849	-0.699	
Ce_2O_3	-3.731	-3.781	-3.72		PtO	-0.37	-0.599	-0.425	
CeO_2	-3.767	-3.95	-3.844		PtO_2	-0.57	-0.945	-0.762	
Co_3O_4	-1.347	-1.421	-1.536	-1.224	Rb_2O	-1.171	-1.12	-1.097	
CoO	-1.232	-1.333	-1.162	-1.338	Re_2O_7	-1.438	-2.053	-1.562	
Cr_2O_3	-2.352	-2.349	-2.609	-2.339	ReO_2	-1.495	-1.917	-1.546	
CrO_2	-2.07	-2.032	-2.345	-2.096	ReO_3	-1.583	-2.16	-1.67	
CrO_3	-1.521	-1.542	-1.713	-1.507	Rh_2O_3	-0.737	-1.095	-1.025	
Cs_2O	-1.195	-1.199	-1.145		RuO_2	-1.054	-1.478	-1.261	
CsO_2	-0.989	-0.975	-0.978		SO_3	-1.136	-1.766	-1.214	

Continued on next page

Table S3 – *Continued from previous page*

Formula	ΔH_{exp}	ΔH_{MP}	ΔH_{SCAN}	ΔH_{SCAN+U}	Formula	ΔH_{exp}	ΔH_{MP}	ΔH_{SCAN}	ΔH_{SCAN+U}
Cu_2O	-0.598	-0.651	-0.519		Sb_2O_3	-1.484	-1.771	-1.441	
CuO	-0.839	-0.955	-0.842		Sb_2O_5	-1.492	-1.771	-1.459	
Dy_2O_3	-3.861	-4.031	-3.972		SbO_2	-1.567	-1.859	-1.55	
Er_2O_3	-3.934	-4.078	-4.014		Sc_2O_3	-3.956	-3.989	-3.925	
Eu_2O_3	-3.447	-3.186	-3.058		SeO_2	-0.778	-1.172	-0.804	
EuO	-3.057	-3.14	-3.097		SiO_2	-3.147	-3.289	-3.087	
Fe_2O_3	-1.711	-1.89	-1.629	-1.699	Sm_2O_3	-3.778	-3.883	-3.8	
Fe_3O_4	-1.66	-1.844	-1.623	-1.629	SnO	-1.455	-1.648	-1.37	
FeO	-1.41	-1.682	-1.306	-1.42	SnO_2	-1.995	-2.129	-1.882	
Ga_2O_3	-2.258	-2.288	-2.098		SrO	-3.068	-3.097	-3.036	
Gd_2O_3	-3.786	-3.913	-3.772		SrO_2	-2.189	-2.211	-2.169	
GeO_2	-2.004	-2.099	-1.784		Ta_2O_5	-3.03	-3.36	-3.102	
HfO_2	-3.861	-4.044	-3.927		Tb_2O_3	-3.866	-4.007	-3.94	
HgO	-0.471	-0.65	-0.355		TbO_2	-3.356	-3.214	-3.03	
Ho_2O_3	-3.899	-4.056	-3.99		TeO_2	-1.093	-1.514	-1.155	
In_2O_3	-1.919	-2.018	-1.871		ThO_2	-4.238	-4.392	-4.25	
IrO_2	-0.862	-1.265	-0.936		Ti_2O_3	-3.153	-3.323	-3.226	
K_2O	-1.255	-1.259	-1.211		Ti_3O_5	-3.186	-3.403	-3.287	
K_2O_2	-1.285	-1.299	-1.248		TiO	-2.812	-2.924	-2.854	
KO_2	-0.983	-0.981	-0.99		TiO_2	-3.261	-3.523	-3.395	
La_2O_3	-3.721	-3.898	-3.803		Tl_2O	-0.578	-0.826	-0.685	
Li_2O	-2.068	-2.074	-2.076		Tl_2O_3	-0.809	-1.122	-0.779	
Li_2O_2	-1.642	-1.654	-1.644		Tm_2O_3	-3.915	-4.112	-4.046	
Lu_2O_3	-3.893	-4.143	-4.081		U_3O_8	-3.368	-3.725	-3.396	
MgO	-3.118	-3.069	-3.051		UO_2	-3.748	-3.781	-3.469	
Mn_2O_3	-1.986	-2.032	-2.183	-2.01	UO_3	-3.171	-3.635	-3.255	

Continued on next page

Table S3 – *Continued from previous page*

Formula	ΔH_{exp}	ΔH_{MP}	ΔH_{SCAN}	ΔH_{SCAN+U}	Formula	ΔH_{exp}	ΔH_{MP}	ΔH_{SCAN}	ΔH_{SCAN+U}
Mn_3O_4	-2.054	-2.067	-2.148	-2.047	V_2O_3	-2.526	-2.538	-2.701	-2.549
MnO	-1.995	-2.004	-1.889	-1.996	V_2O_5	-2.295	-2.306	-2.485	-2.283
MnO_2	-1.8	-1.814	-2.155	-1.778	VO_2	-2.466	-2.49	-2.673	-2.483
MoO_2	-2.031	-2.142	-2.077	-2.03	WO_2	-2.037	-2.033	-2.109	
MoO_3	-1.931	-2.029	-2.133	-1.932	WO_3	-2.183	-2.189	-2.329	
Na_2O	-1.444	-1.439	-1.412		Y_2O_3	-3.949	-3.99	-3.972	
Na_2O_2	-1.33	-1.303	-1.279		ZnO	-1.816	-1.801	-1.656	
NaO_2	-0.901	-0.903	-0.913		ZrO_2	-3.803	-3.838	-3.845	

Table S4: Calculated and experimental formation enthalpies (eV/atom) of 47 ternary oxides. ΔH_{SCAN+U} are data calculated using the SCAN+U functional. ΔH_{MP} are the PBE(+U) data retrieved from the Materials Project.[1–3] The experimental data were from Ref 4, 5, 7

Compound	ΔH_{exp}	ΔH_{MP}	ΔH_{SCAN+U}	Compound	ΔH_{exp}	ΔH_{MP}	ΔH_{SCAN+U}
Al_2CoO_4	-2.882	-2.895	-2.897	$Mg_2V_2O_7$	-2.671	-2.698	-2.694
Al_2CuO_4	-2.882	-2.671	-2.607	$MgCr_2O_4$	-2.632	-2.629	-2.603
Al_2FeO_4	-2.912	-2.833	-2.726	$MgMoO_4$	-2.419	-2.486	-2.413
Al_2NiO_4	-2.843	-2.711	-2.583	MgV_2O_6	-2.534	-2.548	-2.546
$BaMoO_4$	-2.619	-2.728	-2.658	$Mn(FeO_2)_2$	-1.819	-1.937	-1.826
BaV_2O_6	-2.628	-2.712	-2.695	$MnAl_2O_4$	-3.11	-3.065	-3.05
$Ca_2Fe_2O_5$	-2.457	-2.541	-2.434	$MnMoO_4$	-2.058	-2.144	-2.109
$Ca_2V_2O_7$	-2.905	-2.929	-2.922	Na_2CrO_4	-1.976	-2.007	-2.017
$Ca_3V_2O_8$	-3.012	-2.993	-3.002	$Na_2Mo_2O_7$	-2.225	-2.183	-2.106
$Ca(FeO_2)_2$	-2.191	-1.89	-2.201	Na_2MoO_4	-2.272	-2.215	-2.171
$CaCr_2O_4$	-2.709	-2.696	-2.691	$Na_4V_2O_7$	-2.421	-2.334	-2.332
$CaMoO_4$	-2.671	-2.715	-2.671	$NaCrO_2$	-2.271	-2.256	-2.264
CaV_2O_6	-2.682	-2.718	-2.688	$NaFeO_2$	-1.809	-1.934	-1.855
Cr_2CoO_4	-2.121	-2.132	-2.135	$NaVO_3$	-2.47	-2.393	-2.378
Cr_2CuO_4	-1.915	-1.94	-1.904	$SrMoO_4$	-2.676	-2.741	-2.686
Cr_2FeO_4	-2.142	-2.232	-2.138	$Ti(FeO_2)_2$	-2.223	-2.347	-2.161
Cr_2NiO_4	-2.037	-1.938	-1.938	$TiCoO_3$	-2.503	-2.663	-2.631
Cs_2CrO_4	-2.116	-2.087	-2.117	$TiFeO_3$	-2.565	-2.818	-2.646
Cs_2MoO_4	-2.243	-2.272	-2.209	$TiMn_2O_4$	-2.591	-2.689	-2.649
Fe_2CoO_4	-1.612	-1.744	-1.652	$TiMnO_3$	-2.817	-2.971	-2.918
$FeCuO_2$	-1.329	-1.452	-1.308	$TiNiO_3$	-2.492	-2.496	-2.57
$FeMoO_4$	-1.831	-2.016	-1.863	$Zn(FeO_2)_2$	-1.746	-1.896	-1.752

Continued on next page

Table S4 – *Continued from previous page*

Compound	ΔH_{exp}	ΔH_{MP}	ΔH_{SCAN+U}	Compound	ΔH_{exp}	ΔH_{MP}	ΔH_{SCAN+U}
K_2CrO_4	-2.058	-2.087	-2.101	$ZnCr_2O_4$	-2.292	-2.272	-2.227
$LiFeO_2$	-1.992	-2.063	-1.996				

Table S5: Calculated and experimental formation Gibbs free energy (eV/formula) of solid and aqueous ions for element Pourbaix diagram studied in this work. The referenced solid of each element Pourbaix diagram are highlighted in bold. The experimental data were obtained from Ref 5, 6, 8, 10

Species	ΔG_{exp}	ΔG_{calc}	Species	ΔG_{exp}	ΔG_{calc}
Ti	0	0	$Fe(OH)_2$[+]	-4.540	-4.465
TiO	-5.130	-5.391	$Fe(OH)_3$(aq)	-6.834	-6.759
Ti_2O_3	-14.865	-15.180	$Fe_2(OH)_2$[4+]	-4.843	-4.692
TiO_2	-9.219	-9.553	FeO_2[-]	-3.817	-3.741
Ti_3O_5	-24.019	-24.710	FeO_4[2-]	-3.339	-3.264
TiH_2	-1.089	-1.250	Co	0	0
Ti[2+]	-3.229	-3.563	**CoO**	-2.125	-2.359
Ti[3+]	-3.595	-3.929	Co_3O_4	-7.278	-7.298
TiO[2+]	-5.934	-6.268	Co_2O_3	-4.992	-3.501
$HTiO_3$[-]	-9.823	-10.157	CoO_2	-2.248	-2.008
TiO_2[2+]	-4.801	-5.136	$Co(OH)_2$	-4.727	-5.020
Ta	0	0	Co[2+]	-0.555	-0.789
Ta_2O_5	-19.808	-20.131	Co[3+]	1.253	1.019
TaO_2+	-8.733	-8.895	$HCoO_2$[-]	-3.598	-3.832
Se	0	0	Ni	0	0
SeO_2	-1.777	-1.779	NiO	-2.194	-2.158
Se[2-]	1.847	1.844	$Ni(OH)_2$	-4.696	-4.848
H_2Se(aq)	0.228	0.225	Ni_3O_4	-7.378	-6.269
HSe[-]	0.453	0.451	Ni_2O_3	-4.868	-2.965
H_2SeO_3(aq)	-4.418	-4.421	**NiO_2**	-2.230	-1.507
$HSeO_3$[-]	-4.267	-4.269	Ni[2+]	-0.480	-0.444
SeO_3[2-]	-3.836	-3.838	NiOH[+]	-2.355	-2.319

Continued on next page

Table S5 – *Continued from previous page*

Species	ΔG_{exp}	ΔG_{calc}	Species	ΔG_{exp}	ΔG_{calc}
$HSeO_4$[-]	-4.688	-4.690	$Ni(OH)_2$(aq)	-4.208	-4.173
SeO_4[2-]	-4.575	-4.578	$Ni(OH)_3$[-]	-6.079	-6.044
H_2SeO_4(aq)	-4.571	-4.573	$Ni(OH)_4$[2-]	-7.709	-7.673
Mn	0	0	$HNiO_2$[-]	-3.619	-3.584
MnO	-3.761	-3.676	NiO_2[2-]	-2.784	-2.748
MnO_2	-4.821	-4.701	NiO(aq)	-1.706	-1.670
Mn_2O_3	-9.132	-9.097	**Ir**	0	0
Mn_3O_4	-13.299	-13.059	Ir_2O_3	-1.821	-
$Mn(OH)_2$	-6.374	-6.378	IrO_2	-1.214	-2.173
Mn[2+]	-2.362	-2.345	IrO_3	-	-1.538
Mn[3+]	-0.850	-0.832	IrO_4[2-]	-2.038	-2.038
MnO_4[2-]	-5.189	-5.172	Ru	0	0
MnO_4[-]	-4.634	-4.617	**RuO_2**	-2.623	-3.149
MnOH[+]	-4.199	-4.181	RuO_4	-1.653	-2.394
$Mn(OH)_3$[-]	-7.715	-7.697	Ru[2+]	1.558	1.032
$HMnO_2$[-]	-5.243	-5.225	Ru[3+]	1.797	1.272
Fe	0	0	Ru(OH)[2+]	-0.529	-1.054
FeO	-2.553	-2.523	H_2RuO_5(aq)	-4.054	-4.580
Fe_3O_4	-10.524	-10.132	$HRuO_5$[-]	-3.372	-3.898
Fe_2O_3	-7.693	-7.542	RuO_4[-]	-2.592	-3.118
Fe[2+]	-0.817	-0.742	RuO_4[2-]	-3.178	-3.703
Fe[3+]	-0.048	0.027	$Ru(OH)_2$[2+]	-2.299	-2.824
FeO_2[2-]	-3.061	-2.985	$Ru(OH)_2$[+]	-2.911	-3.437
FeOH[+]	-2.874	-2.799	$Ru_4(OH)_{12}$[4+]	-19.453	-21.555

Continued on next page

Table S5 – *Continued from previous page*

Species	ΔG_{exp}	ΔG_{calc}	Species	ΔG_{exp}	ΔG_{calc}
FeOH[2+]	-2.380	-2.304	RuO_4(aq)	-1.596	-2.122
$FeHO_2$[-]	-3.916	-3.841	-	-	-

References

(1) Jain, A.; Ong, S. P.; Hautier, G.; Chen, W.; Richards, W. D.; Dacek, S.; Cholia, S.; Gunter, D.; Skinner, D.; Ceder, G.; Persson, K. A. Commentary: The materials project: A materials genome approach to accelerating materials innovation. *APL Materials* **2013**, *1*, 011002.

(2) Ong, S. P.; Richards, W. D.; Jain, A.; Hautier, G.; Kocher, M.; Cholia, S.; Gunter, D.; Chevrier, V. L.; Persson, K. A.; Ceder, G. Python Materials Genomics (pymatgen): A robust, open-source python library for materials analysis. *Computational Materials Science* **2013**, *68*, 314–319.

(3) Ong, S. P.; Cholia, S.; Jain, A.; Brafman, M.; Gunter, D.; Ceder, G.; Persson, K. A. The Materials Application Programming Interface (API): A simple, flexible and efficient API for materials data based on REpresentational State Transfer (REST) principles. *Computational Materials Science* **2015**, *97*, 209–215.

(4) O. Kubaschewski, C. B. Alcock, and P. J. Spencer, *Materials thermochemistry*, 6th ed.; Pergamon Press, 1993.

(5) P.J. Linstrom and W.G. Mallard, E. *NIST Chemistry WebBook, NIST Standard Reference Database Number 69*; National Institute of Standards and Technology, Gaithersburg MD, 20899, https://doi.org/10.18434/T4D303, (retrieved May 18, 2020), 2020.

(6) Wagman, D. D.; Evans, W. H.; Halow, I.; Parker, V. B.; Bailey, S. M.; Schumm, R. H.; (U.S.), I. f. B. S.; of Standards, U. S. N. B.; of Commerce, U. S. D. *Selected Values of Chemical Thermodynamic Properties*; NBS technical note; United States Department of Commerce, National Bureau of Standards, 1966.

(7) Jain, A.; Hautier, G.; Ong, S. P.; Moore, C. J.; Fischer, C. C.; Persson, K. A.; Ceder, G. Formation enthalpies by mixing GGA and GGA+U calculations. *Physical Review B* **2011**, *84*, 45115.

(8) Pourbaix, M. *Atlas of Electrochemical Equilibria in Aqueous Solutions.*, 2nd ed.; National Association of Corrosion Engineers, 1974: NACE.

(9) Barin, I.; Gregor, P. Thermochemical data of pure substances. 3rd. *Edition, VCH* **1995**,

(10) Rard, J. A. Chemistry and thermodynamics of ruthenium and some of its inorganic compounds and aqueous species. *Chemical Reviews* **1985**, *85*, 1–39.